 FDMP, vol.1, no.1, pp.63-80, 2005

# Phase Distribution of Bubbly Flows under Terrestrial and Microgravity Conditions

**Asghar Esmaeeli**[1]

**Abstract:** We use direct numerical simulations to study phase distribution of bubbles under terrestrial and microgravity conditions. The full Navier-Stokes and energy equations, for the flows inside and outside the bubbles, are solved using a front tracking/finite difference technique. Both nearly spherical and deformable bubbles are considered. For buoyancy-driven flows, spherical bubbles at $Re = \mathrm{O}(10)$ and deformable ones at $Re = \mathrm{O}(100)$ exhibit a uniform spatial distribution at quasi steady-state conditions, while nearly spherical bubbles at $Re = \mathrm{O}(100)$ form horizontal rafts. Bubbles, driven by thermocapillary effects in microgravity, also form horizontal rafts, but due to an entirely different mechanism. When thermocapillary and buoyancy forces act in opposite directions, the raft formation is prevented and the bubbles form a large cluster that moves in the direction of buoyancy.

## 1 Introduction

Bubbles and drops are central to many industrial and natural processes. Heat transfer through boiling is the preferred mode in most power plants and bubble-driven circulation systems are used in metal processing operations such as steel making, ladle metallurgy, and the secondary refining of aluminum and copper. Generally, bubbly flows consist of a large number of bubbles moving in a highly unsteady manner, and considerable effort has been devoted over recent years to the development of engineering models able to describe the mean motion.

Under terrestrial conditions, buoyancy is the major force. Accordingly, buoyancy-driven motion of bubbles continues to be the focus of many studies. Buoyancy, however, is not the only force and in a typical bubbly flow, other forces such as electrophoresis, electrohydrodynamics (EHD), and thermocapillarity, may exist as well. These are regarded as "secondary" forces in many situations because of their relatively small intensity compared to buoyancy. They may, however, influence the fluid dynamics considerably. For example, solutocapillary forces that arise due to the accumulation of surfactants (present in tap water) at the interface of bubbles, tend to immobilize the phase boundary. This, in turn, alters the dynamics substantially (bubbles/drops behave more like solid particles; Harper, 1973). The common feature of almost all of these forces is the alteration of surface tension that acts at the phase boundary. Although, these effects may be undesirable in some cases, they can be used to our advantage in other applications. For example, for bubbly flows in horizontal pipes or motion of neutrally buoyant bubbles/drops, where buoyancy is no longer the dominant force, these effects can be used for a better control of the dispersed phase.

The behavior of a gas bubble rising due to buoyancy or thermocapillarity is reasonably well understood (Clift *et al.*, 1978; Subramanian, 1992). In many practical applications, however, it is the collective behavior of the bubbles that is of interest. Here, we are interested in phase distribution of "freely evolving" array of bubbles. A freely evolving array consists of bubbles that interact freely and can take different rise velocities (i.e., their spatial distribution evolves continuously). This is in contrast to a "regular array" where the bubbles all have the same velocity and their spatial distribution essentially remains constant. Although a regular array is a highly idealized configuration, it has been used in the past by many investigators because of its relative simplicity in mathematical modeling (in the limit of potential and Stokes flow) and numerical simulation. A regular array cannot capture the highly unsteady nature of the flow, however, it may provide good approximations for some flow quantities such as the mean rise velocity. To make the analysis simpler, we consider only monodispersed bubbly flows and we also do not allow for coalescence of bubbles. Such an

[1] Corresponding author: Tel.: 618-453-7001; Fax: 618-453-7685, E-mail address: esmaeeli@engr.siu.edu, Department of Mechanical Engineering and Energy Processes, Southern Illinois University, Carbondale, IL 62901

assumption is supported by the fact that frame by frame analysis of earlier results showed that although bubbles may come momentarily close to each other, actual contact is very rare.

For buoyancy-driven bubbles, we use a fully periodic domain and perform our three-dimensional computations in a reference cell. The flow is initially quiescent and motion is triggered by buoyancy. As the bubbles originally inside the reference cell leave through one boundary, new ones come in through the opposite boundary. Although the motion is unsteady, the simulations are carried out for a long enough time so that a time-averaged behavior of the system is well-established. Here, the governing parameters are the densities ($\rho_l$, $\rho_b$) and the viscosities ($\mu_l$, $\mu_b$) of the ambient liquid and the bubbles, the surface tension coefficient $\sigma$ (which taken to be constant), the spherical volume-equivalent (initial) diameter of the bubbles $d_e$, and the number of the bubbles $N_b$. The rise velocity of the bubbles $W_b$ is the most important dependent variable. Nondimensionalization results in the Reynolds number $Re = \rho_l W_b d_e/\mu_l$ as a function of the Eötvös number $Eo = \rho_l g d_e^2/\sigma$, the Morton number $Mo = g\mu_l^4/\rho_l\sigma^3$, void fraction $\alpha = N_b\pi d_e^3/6L^3$ ($L$ being the domain size), and ratio of the material properties; $\rho_b/\rho_l$ and $\mu_b/\mu_l$. For given fluids, the Eötvös number is a characteristic of the bubble size and the Morton number is a constant representing the viscosity of the liquid. Since both fluids are assumed to be incompressible, $\alpha$ is constant throughout the simulation, and since the bubbles are not allowed to coalesce, $N_b$ remains constant.

For thermocapillary-driven bubbles at zero gravity, the simulations are carried out for two-dimensional systems. In such a case, the reference cell is periodic in the horizontal direction but wall-bounded in the vertical direction. Initially, the flow field is quiescent, and a constant temperature gradient is imposed along the vertical direction. The individual parameters that govern this problem are the effective bubble radius $a = d_e/2$, the surface tension $\sigma$, the surface tension gradient $\sigma_T = d\sigma/dT$, the densities ($\rho_l$, $\rho_b$), the viscosities ($\mu_l$, $\mu_b$), the heat conductivities ($k_l$, $k_b$), the heat capacities ($c_l, c_b$), and the imposed temperature gradient $|\nabla T_\infty| = |T_t - T_b|/L$, where $T_t$, $T_b$, and $L$ are the temperatures of the top and the bottom walls and the separation distance of the walls, respectively. Nondimensionalization results in $Re_T = u_s a/\nu_l$, $Ma = u_s a/\alpha_l$, $Ca = u_s\mu_l/\sigma_{ave}$, void fraction (as defined before), and the ratio of material properties, $\rho_b/\rho_l$, $\mu_b/\mu_l$, $k_b/k_l$, and $c_b/c_l$, as the governing nondimensional parameters. Here, $u_s = |\sigma_T\nabla T_\infty|a/\mu_l$ is a reference velocity, derived by considering the fact that the flow is caused by the variation of interfacial tension created by thermal gradient. $\nu_l$ and $\alpha_l$ are the kinematic viscosity and the thermal diffusivity of the ambient fluid, respectively. $Re_T$ is the Reynolds number based on the scale velocity, $Ma$ is the Marangoni number that is the ratio of convective transport of energy to heat transfer by molecular diffusion, and $Ca$ is the capillary number (an indicator of bubble deformation). When buoyancy is also present, $\Pi = |\sigma_T\nabla T_\infty|/(\rho_l - \rho_b)ga$ is introduced as an additional nondimensional number, characterizing the relative importance of buoyancy and surface tension.

## 2 Background

In what follows, we will briefly review some of the previous studies on phase distribution of bubbles. We make no attempt to cite every paper, but have selected a few critical and/or representative analyses.

### *2.1 Buoyancy-driven bubbly flow*

The state of a bubbly system – as well as other particulate flows – depends strongly on the microstructure of the dispersed phase. Previous experimental and numerical studies of suspensions of solid particles (Bossis & Brady, 1984), liquid drops (Zhou & Pozrikidis, 1993), and bubbles (Esmaeeli & Tryggvason, 1998, 1999) have shown that the rheological properties of the suspension, such as the effective viscosity and the average rise velocity of the particles, can be well-correlated with the spatial distribution of the particles. Brady & Bossis (1985), for example, showed that the effective viscosity of a suspension of rigid spheres at high volume fraction is determined, primarily, by the strong lubrication forces associated with cluster formation.

For buoyancy-driven bubbly flows, in the absence of an imposed pressure gradient, shear, and other external forces, one may generally expect to see a "random" distribution of the bubbles at quasi steady-state conditions (hereafter also referred to as "uniform" distribution to distinguish it from the cases in which coherent structures of aligned bubbles are formed, e.g., raft or columnar structures). Therefore, a random distribution has been often used as a reference structure. The motion of a bubble in a swarm tends to be influenced by the motion of bubbles at short separation distances as a result of direct interactions, and by the long range hydrodynamic forces of the bubbles at larger separation distances. In both limits, however, the problem becomes simpler if one focuses on the pairwise interactions of particles. It is, therefore, not surprising that a vast body of literature has been devoted to the binary interactions of particles and to a lesser extent to their ternary interactions. In particular, for the two limiting cases of potential and Stokes flow, where it is possible to linearize the Navier Stokes equation, the binary interactions have been studied analytically as well as numerically in great detail. See, for example, Lamb (1932) for potential flow solutions and Happel & Brenner (1965) and Kim & Karrila (1991) for Stokes flow solutions. In general, the central theme of these studies has been calculation of the average rise velocity and/or the drag coefficients for two fundamental modes of interactions (i.e., spheres rising in tandem and side-by-side) and comparison of the results with the corresponding ones for a solitary sphere.

In this study, we are interested in bubbly flows at finite Reynolds number where both inertia and viscous forces are important. For this flow, Esmaeeli & Tryggvason investigated the motion of nearly spherical bubbles at moderate Reynolds numbers in a number of papers and here we briefly review some of their results. Esmaeeli and Tryggvason (1998) investigated a case where the average rise Reynolds number of the bubbles remained relatively small $(1-2)$ and Esmaeeli and Tryggvason (1999) looked at another case where the Reynolds number was $20-30$. In both cases, most of the simulations were limited to two-dimensional flows, although a few simulations for three-dimensional systems with up to eight bubbles were included. Simulations of freely evolving arrays were compared with regular arrays and it was found that while freely evolving bubbles at low Reynolds numbers rise faster than a regular array (in agreement with Stokes flow results), at higher Reynolds numbers the trend is reversed and the freely moving bubbles rise slower. These simulations showed that at finite Reynolds numbers, two-bubble interactions take place by the "drafting, kissing, and tumbling" mechanism predicted by Fortes, Joseph, and Lundgren (1987) for solid particles: "For two bubbles rising in tandem, the lower one is in the wake of the one in front and is shielded from the oncoming fluid. It therefore experiences less drag but the same buoyancy force, and moves faster than the one in front. An in-line configuration of two touching bubbles is inherently unstable, and the bubbles "tumble" whereby the bottom one catches up with the top one. At the end of the tumbling the bubbles move apart." The time averages for the two-dimensional bubbles were generally well-converged but exhibited a dependency on the size of the system. This dependency was stronger for the low Reynolds number case than that for the moderate Reynolds number one. Although many of the qualitative aspects of the interactions of a few three-dimensional bubbles were captured by simulations of two-dimensional bubbles, there were some quantitative differences between the results for two- and the three-dimensional systems. Examination of the pair distribution function for the bubbles showed a mild preference for horizontal alignment of bubble pairs at short separation distances, independent of system size, but the distribution of bubbles showed a tendency to remain nearly uniform (random).

To examine a much larger number of three-dimensional bubbles, Bunner and Tryggvason (2002*a*) developed a parallel version of the method used by Esmaeeli and Tryggvason (1998). Their largest simulations followed the motion of 216 three-dimensional buoyant bubbles per periodic domain for a relatively long time. The governing parameters were selected such that the average rise Reynolds number was about $20-30$ (comparable to Esmaeeli and Tryggvason, 1999, but not identical), depending on the void fraction, and deformations of the bubbles were small. These simulations confirmed earlier observations of Esmaeeli & Tryggvason (1998, 1999) and in particular, showed that there is an increased tendency for the bubbles to line up side-by-side as the rise Reynolds number increases.

### *2.2 Thermocapillary-driven flow*

Motion of bubbles/drops as a result of variations of surface tension with temperature is often referred to as thermocapillary migration. The study of the phenomenon is motivated by its potential applications in space operations where thermocapillary effects can be used as a possible mechanism for vapor bubble control (Ostrach, 1982). Even on earth, thermocapillary forces can be used to control motions of droplets of very small size or of nearly equal density with ambient fluid. The problem was first studied both experimentally and theoretically by Young *et al.* (1959). In their experiments with air bubbles in viscous silicone oil, they were able to hold a bubble stationary by using a downward temperature gradient. They found the migration velocity, $U_b$, of a fluid sphere in an infinite domain due to a linear temperature field and in the limit of zero convective transport of momentum and energy, to be:

$$U_b = \frac{2}{\mu_l(2+3\gamma)}\left(\frac{\sigma_T \nabla T_\infty a}{2+\eta} - \frac{\Delta\rho g a^2(1+\gamma)}{3}\right), \quad (1)$$

where $\eta = k_b/k_l$, $\gamma = \mu_b/\mu_l$, and $\Delta\rho = \rho_l - \rho_b$. This equation predicts that at zero gravity, the migration velocity is independent of fluid density and heat capacity, inversely proportional to the ratio of heat conductivity of bubbles to that of ambient fluid, and directly proportional to the bubble size, the surface tension gradient, and the initial temperature gradient. Crespo & Manuel (1983) and Balasubramaniam & Chai (1987) showed that equation (1) is an exact solution for the full Navier-Stokes equations for any value of the Reynolds number as long as convective transport of energy is negligible.

Because of inherent difficulties in performing microgravity experiments, experimental results have considerably lagged behind the theoretical analysis. The focus of most of the studies, however, has been quasi-steady motion of a single bubble/drop or interactions of a few of them under preassigned orientations, and in the limit of zero Reynolds and Marangoni numbers. While these studies are quite useful for the illustration of qualitative effects, they are unable to provide information on the dynamics of a real flow. The overall picture that emerges from these investigations is that for a given fluid and bubble size, thermocapillary forces are much weaker than the buoyant forces, and they also decay faster with increasing distance from the bubble. For a detailed discussion of the early studies of a single bubble/drop, see Subramanian (1992), and for a review of the investigations on bubble/bubble interactions, see Nas & Tryggvason (2003). Here, we only mention the remarkable work of Acrivos *et al.* (1990) who showed that the terminal velocity of a random distribution of bubbles, in a confined domain and in the limit of zero *Re* and *Ma*, decreases linearly with an increase in the void fraction. We note that this result is similar to the corresponding one for sedimentation velocity of rigid particles in Stokes flow (Batchelor, 1972).

For interaction of bubbles/drops at finite Reynolds and Marangoni number, the literature is limited to the computations of Nas (1995) for multibubbles, and Nas & Tryggvason (1993, 2003) for two bubbles/drops: "For two bubbles rising in tandem in an upward temperature gradient, the bubble on the top, pumps the high temperature ambient fluid from the top to the bottom. This results in an increase in the temperature of the fluid in the gap between the bubbles which leads to a decrease (respectively increase) in the temperature gradient across the top (respectively bottom) bubble. As a result, the velocity of the bubble in the wake increases while the velocity of the one on the top decreases. The bubble in the wake catches up with the top one, they nearly touch, and then, separate." If the void fraction is high enough, this process may lead to formation of horizontal layers of bubbles which in turn results in a substantial decrease in the mean velocity of the bubbles. Esmaeeli *et al.* (1996, 1997) and Esmaeeli & Arpaci (1999) investigated the effect of shear forces and bubble/bubble coalescence on the multibubble dynamics and found that both effects tend to prevent the raft formation, and thereby, the subsequent decrease in the mean velocity. The role played by possible thermal wake effects in the case of many interacting droplets driven by thermocapillary forces was considered by Lappa (2005) within the framework of studies devoted to the investigation of immiscible metallic alloys.

## 3 Mathematical Formulation and Numerical Method

Consider a domain consisting of bubbles dispersed in a liquid. The fluids inside and outside of the bubbles are Newtonian and immiscible, and the material properties in each fluid are constant but different from one another. The fluid motion both inside and outside the bubbles is governed by equations of conservation of mass, momentum, and energy, where the corresponding equations in each fluid are coupled together through the jump conditions at the phase boundary. Rather than writing the governing equations separately for each of the fluids along with the jump conditions at the interface, we use a "one-field" formulation which is valid for the entire flow field and satisfies the correct jump conditions at the phase boundary. This is achieved by adding the appropriate source terms to the conservation laws in the form of delta functions localized at the interface.

For buoyancy-driven motion of bubbles in isothermal flow fields, or under conditions where the temperature is a passive scalar, one can bypass the energy equation. The Navier-Stokes equations, valid for the entire domain and incorporating the jump conditions at the interface are:

$$\rho\left(\frac{\partial \mathbf{u}}{\partial t}+\nabla\cdot\mathbf{uu}\right)=-\nabla p+\rho\mathbf{g}+\nabla\cdot\mu(\nabla\mathbf{u}+\nabla\mathbf{u}^T)+\mathbf{F}_s. \tag{2}$$

Here, $\mathbf{u}$ is the velocity, $p$ is the pressure, $\rho$ and $\mu$ are the discontinuous density and viscosity fields, respectively, $\mathbf{g}$ is the gravitational acceleration, and $\mathbf{F}_s$ is the surface force

$$\mathbf{F}_s=\sigma\int_F \kappa'\mathbf{n}'\delta(\mathbf{x}-\mathbf{x}')dA', \tag{3}$$

distributed at the grid points as a body force. The primed parameters are evaluated at the bubble surface: $\kappa'$ is twice the mean curvature, $\mathbf{n}'$ is a unit vector normal to the bubble surface pointing into the bubble, $\mathbf{x}'$ is the coordinate of a point on the bubble, and $dA'$ is the surface element. $\sigma$ is the surface tension coefficient and $\delta$ is a three-dimensional delta function constructed by repeated multiplication of one-dimensional delta functions. $\mathbf{x}$ is the point at which the Navier-Stokes equations are evaluated.

In numerical implementation, the surface tension on each element (i.e., $\sigma\kappa\mathbf{n}$) is computed using a conservative method which assures that the total force on a closed surface is zero. This is important for long time simulations, since even small errors can lead to a net force that moves the bubbles in an unphysical way. The method is based on the fact that it is possible to convert the area integral of the curvature into a contour integral over the edges of the element (see Weatherburn, 1927) and compute the total surface force on each element (which is what is actually required) directly by:

$$\kappa\mathbf{n}dA=\oint_e \mathbf{t}\times\mathbf{n}dS, \tag{4}$$

where $\mathbf{t}$ is a unit vector tangent to the edge of the element, and $S$ is an arclength coordinate.

Both the bubbles and the ambient fluid are taken to be incompressible, so the velocity field is divergence free:

$$\nabla\cdot\mathbf{u}=0. \tag{5}$$

Combining the momentum equation and the incompressibility condition leads to a non-separable elliptic equation for the pressure. We also have equations of state for the fluid properties:

$$\frac{D\phi}{Dt}=0, \tag{6}$$

where $\phi=\{\rho,\mu\}$. Here, $D/Dt$ is the material derivative and this equation simply states that the density and the viscosity of each fluid remains constant.

The above equations are solved by a second order space-time accurate front tracking/finite volume method on a staggered grid. The method has been described in detail by Unverdi & Tryggvason (1992) and improvements to the basic method including a few validations tests are described in Esmaeeli & Tryggvason (1998). The current computations are done using a parallel version of the code, developed by Bunner & Tryggvason (2002*a*) and modified by Esmaeeli & Tryggvason (2005), that is well-suited for large scale simulations of bubbly flows at high Reynolds number.

For thermocapillary-driven flows, in addition to the momentum equation, we also need to solve the energy equation:

$$\rho c\left(\frac{\partial T}{\partial t}+\nabla\cdot\mathbf{u}T\right)=\nabla\cdot k\nabla T. \tag{7}$$

Here, the surface tension coefficient is no longer constant and is a function of the temperature. To account for the variations of the surface tension with the temperature, we use a linear model:

$$\sigma=\sigma_0+\sigma_T(T-T_0), \tag{8}$$

where, $\sigma_0$ is the surface tension at a reference temperature $T_0$ and $\sigma_T=d\sigma/dT$. $\sigma_T$ is negative for most fluids, therefore, increasing the temperature reduces the surface tension. The above model is reasonable for flows with small temperature gradient. We also need to modify equation (3) to take into account tangential surface tension effects:

$$\mathbf{F}_s=\int_F(\sigma\kappa'\mathbf{n}'+\nabla'_s\sigma)\delta(\mathbf{x}-\mathbf{x}')dA'. \tag{9}$$

Here, $\nabla_s=\nabla-\nabla_n$ is the surface del operator, where $\nabla_m=\mathbf{n}\cdot\nabla$. In numerical implementation, the surface tension is computed by:

$$(\sigma\kappa\mathbf{n}+\nabla_s\sigma)dA=\oint_e\sigma\mathbf{t}\times\mathbf{n}dS, \tag{10}$$

which takes into account the fact that $\sigma(T(S))$ varies over the edges of the element. Finally, $\phi$ (used in equation (6)) is generalized to include $k$ and $c$ in addition to $\rho$ and $\mu$; $\phi=\{\rho,\mu,c,k\}$.

The above equations are solved explicitly by solving the energy equation first for the temperature field, calculating the surface force using the updated temperature, and finally computing the new velocity field by solving the Navier-Stokes equations.

## 4 Results

### *4.1 Buoyant rise of bubbles*

The simulations presented in this section deal with fully periodic domains. The bubbles can cross the boundaries, so their motions can be followed indefinitely. The goal is, however, to simulate the flow for a time sufficiently long to guarantee quasi steady-state conditions; a state where the mean rise velocity remains essentially unchanged. For these domains, we also need to impose an additional constrain to prevent uniform downward acceleration of the whole flow field. This is achieved by subtracting the force $\rho_0 \mathbf{g}$ from the right hand side of the Navier-Stokes equations, where $\rho_0 = \alpha\rho_b + (1-\alpha)\rho_l$ is the spaced-averaged density. This ensures that the net flux of vertical-momentum through the computational domain is zero. If the bubbles were completely massless, this would be equivalent to imposing no net through-flow of liquid. Here, however, a small net through-flow sometimes develops since mass is not conserved exactly. All our results have been corrected by subtracting this through-flow, and the rise velocity of the bubbles therefore represents the relative velocity with respect to a stationary liquid.

We start by considering the behavior of a system of 48 spherical bubbles rising in a $3\times3\times3$ domain and resolved by a $256^3$ grid. For this flow, $Eo = 0.5$, $Mo = 10^{-6}$, $\alpha = 5.86\%$, and $\rho_b/\rho_l = \mu_b/\mu_l = 1/20$. These values of the Eötvös and the Morton numbers correspond, for instance, to an air bubble of a diameter 1.65 mm rising in an aqueous solution of sugar in water of sugar/water mass fraction of 0.4486 ($\rho = 1195.6$ kg m$^{-3}$, $\mu = 0.011$ N s m$^{-2}$, $\sigma = 0.0642$ N m$^{-1}$; Stewart, 1995). The actual density and viscosity ratio, however, would be lower than those used in our numerical simulations. This, however, does not lead to important differences with respect to a real situation as the dynamics is a weak function of the property ratios. Figure (1) shows two frames from this simulation at an early time and at (essentially) a steady-state time along with the trajectories of the bubbles. Initial conditions correspond to bubbles set in the vertices of a $3\times4\times4$ cube with their positions perturbed randomly. The initial distribution tends to be quite stable during the early stages of evolution since the bubbles move with almost the same velocity. This is very clear in the first frame which shows the bubbles as they are about to leave the first period. However, the initial set up breaks up eventually as a result of the aforementioned drafting, kissing, and tumbling between bubbles rising in the same columns. The outcome is a seemingly random (uniform) distribution of the bubbles, spreading over two periodic boxes in the vertical direction (second frame). Once the array breaks up, other modes of interactions are involved in the process. In the top frame, for example, one can identify a few of the bubbles in side-by-side, tandem, or in-between arrangements. The overall motion is, however, mainly in the direction of buoyancy, as no bubble has crossed the periodic boundaries in the horizontal directions. Since the surface tension is high enough, the bubbles remain spherical. Examination of the trajectories of the bubbles shows that the bubbles have risen in nearly straight paths. During this time, the centroid of the bubbles has risen about $34d_e$.

The mean rise velocity of the bubbles is perhaps the most important parameter that characterizes the bubbly flows and in figure (2) we show the evolution of this parameter for this simulation and another companion simulation with 14 bubbles which has been run for a longer time. The 14-bubble simulation was run in a $2\times2\times2$ domain and it has the same nondimensional numbers and the same grid resolution per bubble diameter as those of the 48 bubble simulation, respectively. At the end of the simulation, the centroid of the 14 bubbles has risen about $86d_e$. It is seen that the large system tends to settle to a quasi steady-state while the smaller one has already reached such a condition. The mean rise velocities of the two systems after the transient (i.e., $t = 50$) are very close which suggests the results are independent of the system size.

In the above simulations ($Re = O(10)$), the bubbles remained spherical and their trajectories were essentially straight. This is not always the case and depending on the range of the physical parameters such as the bubble size, the properties of ambient fluid, etc., bubbles may deform and rise in zigzag or spiral paths. The deformation of bubbles can lead to profound changes in the dynamics because of introduction of new modes of interaction. The literature on the motion of deformable bubbles

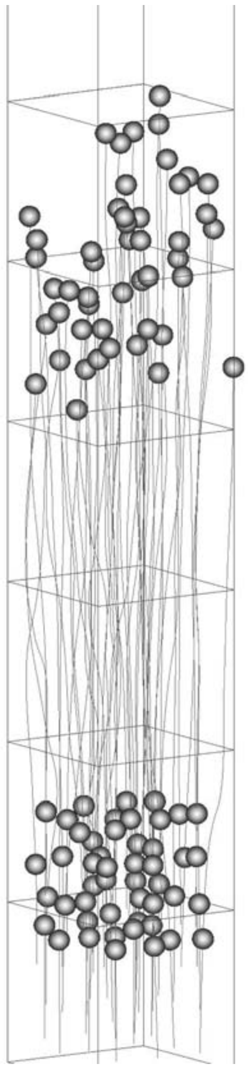

**Figure 1** : Spatial distributions of 48 spherical bubbles at an early time ($t = 7.53$) and at $t = 53.5$. The figure also shows the paths of the centroids of the bubbles. Here, $Eo = 0.5$, $Mo = 10^{-6}$, and $\alpha = 5.86\%$.

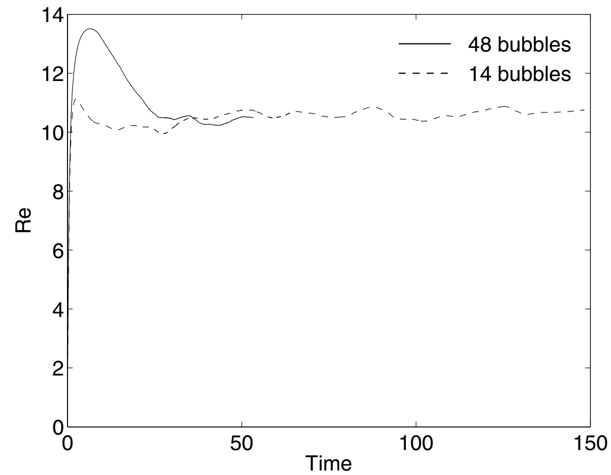


**Figure 2** : Evolution of the mean rise velocities of the 48 and 14 bubbles at $Eo = 0.5$ and $Mo = 10^{-6}$.

is more limited than that of the spherical ones, primarily because of complexities in dealing with deformable particles. Here, we only mention a study by Bunner & Tryggvason (2003) who compared interactions of 27 deformable and nearly spherical bubbles at a Reynolds number of about 20 and void fraction of 6%. One of their main observations was that the deformation results in a significant modification of the bubble microstructure as a result of a reversal in the direction of the lift force. This effect leads to the accumulation of the bubbles in a column. Bunner & Tryggvason (2003) called this phenomenon a "streaming state" and showed that the average rise velocity of the deformable bubbles increases dramatically as a result of the formation of streams.

Here, we simulate motion of 14 deformable bubbles at $Eo = 4$, $Mo = 10^{-6}$, and $\alpha = 5.86\%$. These values of the Eötvös and the Morton numbers correspond to a 4.674 mm bubble rising in the same fluid as that in figure (1). To "accelerate" the possible onset of the streaming behavior, initially the bubbles are set in four columns (their positions are perturbed slightly). In the absence of the streaming instability, the initial configuration should be replaced by a more random (uniform) one as a result of drafting, kissing, and tumbling mechanisms illustrated before, whereas the streaming instability should force the bubbles to rise retaining their original columnar distribution. Figure (3) shows the results of this investigation. The first frame shows the initial positions of the bubbles and the subsequent frames show the bubbles, velocity vectors, and vorticity contours (in a plane cut through the middle of the domain) at an early and a later time. The shaded bubbles are located in the space behind the considered plane. As expected, during an initial stage of the process, the bubbles tend to rise maintaining their initial columnar arrangement (second frame), but then disperse over the entire domain (third frame). This result is in apparent contrast to that of Bunner & Tryggvason (2003). To find out the reason(s), we have performed a frame by frame analysis of the bubbles distributions at different times, examined their trajectories, and made an animation of their motions. These investigations show that the difference in the behavior of the systems is due to the development of path (and shape) instabilities in our simulation, while the deformable bubbles in Bunner & Tryggvason (2003) were featured by a quasi-steady deformation and rose in straight paths. Although bubble deformation in our simulation tends to trigger streaming behavior, just as it was the case in Bunner & Tryggvason (2003), this tendency is greatly weakened by a "wobbling" effect. The final outcome is, therefore, the emergence of a random/uniform distribution of the bubbles, albeit at a time scale larger than that for nearly spherical ones. The path and shape instabilities of the bubbles in our simulation can be clearly seen in figure (4) which shows the evolution of rise Reynolds number ($Re = \mathrm{O}(100)$) and the surface area (scaled by initial bubble surface area $A_0$) of the individual bubbles. Both quantities are highly oscillatory with large standard deviations.

To compare the dynamics of spherical bubbles at high Reynolds number with that of deformable ones, we have performed another simulation of motion with 14 bubbles at $Eo = 0.5$ and $Mo = 1.95 \times 10^{-9}$ and with the same initial positions as those in the first frame of figure (3). The $Eo$ and $Mo$ are chosen so that a single bubble at these parameters remains spherical while its rise Reynolds number is comparable to that of a deformable bubble at $Eo = 4$ and $Mo = 10^{-6}$ (i.e., $Re = \mathrm{O}(100)$) (see, Clift *et al.*, 1978). In such a case, the Eötvös and the Morton numbers correspond to an air bubble of a diameter of about 1.71 mm in aqueous solution of sugar in water of sugar/water mass fraction of 0.274 ($\rho = 1110$ kg m$^{-3}$, $\mu = 0.0028$ N s m$^{-2}$, $\sigma = 0.064$ N m$^{-1}$; Stewart, 1995). Figure (5) shows the result of this investigation. The first frame shows the bubbles at an early time and the remaining frames show the bubbles at quasi steady-state conditions. The initial array breaks up and is replaced by a uniform distribution of bubbles (first frame). However, as time passes, the uniform distribution evolves to a horizontal layer of bubbles or "rafts." Two layers are clearly shown in the second and the third frames where we can identify a collection of nine and thirteen bubbles at the edges of the domain, respectively. Similar rafts have been predicted by potential flow simulations (Sangani and Didwania ,1993; Smereka ,1993). However, so far they have not been fully supported by experiments. Although the Reynolds number is finite, we believe that this is a potential flow effect as was demonstrated by Esmaeeli & Tryggvason (2005). They examined motion of three bubbles initially set in a perturbed row, at the above Morton number ($Mo_1 = 1.95 \times 10^{-9}$) and at $Mo_2 = 5 \times 10^{-8}$, and $Mo_3 = 5 \times 10^{-5}$ while keeping $E_0 = 0.5$. The rafting took place immediately in the first case, was delayed in the second case, and never occurred in the third case." It should be mentioned that while the bubbles in figure (5) remain nearly spherical, their paths (not shown here) are oscillatory.

As mentioned before, the simulations in figures (3) and (5) were run for a short time only to investigate the onset of streaming behavior. Two additional simulations at the same nondimensional numbers but with a random (uniform) initial distribution of bubbles and for a longer time have been carried out to extend the results shown in figure (2) to the case of deformable bubbles and a larger value of the Reynolds number, respectively. Figure (6) compares the mean rise velocity for these systems and the one introduced earlier in figure (2). The rise velocity of high Reynolds number spherical bubbles consists of waves of high and low frequencies. The low frequency waves are related to the formation and the destruction of the rafts and the high frequency ones are related to random interactions of bubbles. The oscillations in the rise velocity of the deformable bubbles are mainly due to random interactions of bubbles. The rise velocity of the low Reynolds number bubbles, on the other hand, is relatively smooth as the bubbles tend to rise in nearly straight paths.

While it is possible to provide some useful qualitative information about microstructure of a flow at a particular time by simply inspecting the bubbles positions at that time, however, a more sophisticated measure is needed to quantify the phase distribution. Perhaps the most commonly used measure is the pair distribution function $g(\mathbf{r})$ which is defined as the probability of finding a bubble center at position $\mathbf{r}$ given that there is a bubble at the origin. Since $g(\mathbf{r})$ in general is a multidimensional function, the interpretation of the results becomes easier if one focuses on the variations of the pair distribution function with one space variable allowed to change and the others fixed. We choose a spherical coordinate $(r, \theta, \phi)$ and consider the center of a test bubble $i$ to be at the origin. $r_{ij}$ is the separation distance between another bubble $j$ and the test bubble measured from the test bubble. $\theta$ is the azimuth angle measured from the vertical axis in the clockwise direction (i.e., $\theta = 0$ and $\pi$ correspond to a

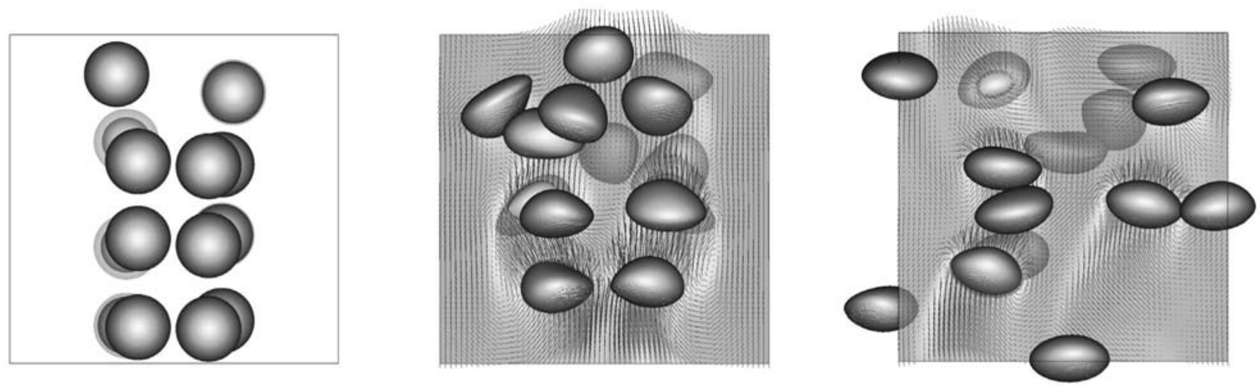

**Figure 3** : Breakup of a columnar array of 14 bubbles at $Eo = 4$ and $Mo = 10^{-6}$. The figure shows the bubbles, the velocity vectors, and the vorticity field at $t = 0$, $t = 6.32$ (when the mean rise velocity is maximum), and at $t = 37.94$ (a quasi steady-state time).

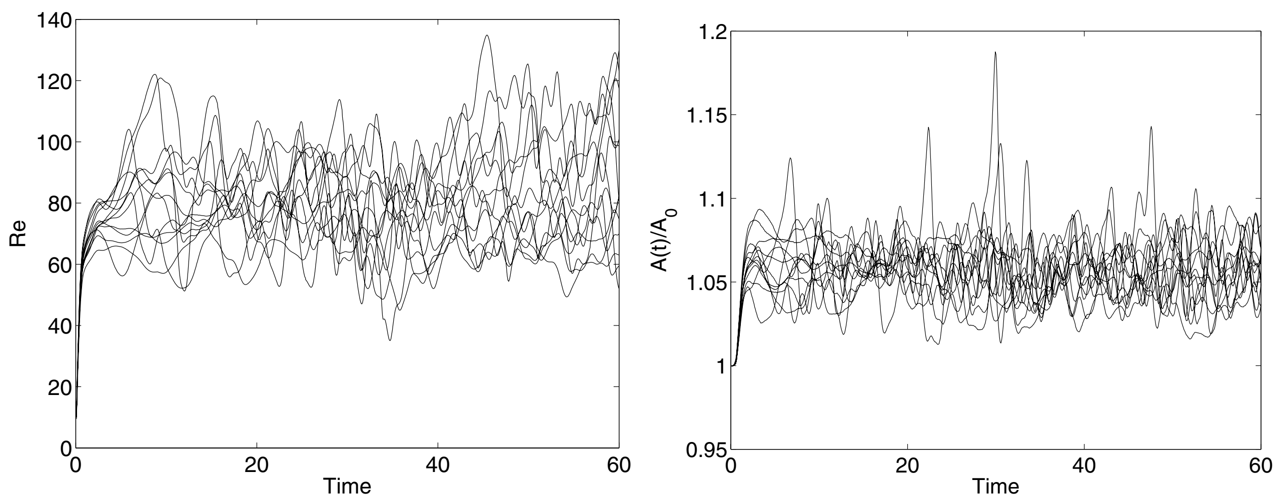


**Figure 4** : Evolution of the rise velocity (left frame) and the surface area (right frame) of the bubbles of figure (3). Here, $A_0$ is the initial bubble surface area.

tandem orientation and $\theta = \pi/2$ corresponds to a side-by-side orientation) and $\phi$ is the polar angle measured from $x$ axis in the counter-clockwise direction. Since the domain is periodic, the variations of $g(\mathbf{r})$ with respect to $\phi$ can be ignored. Therefore, we will be concerned only with changes of the microstructure in the radial ($0 < r < L$) and the azimuthal ($0 < \theta < \pi$) directions, where $L^3$ is the size of the cubic box. The radial and angular distributions are related to $g(r)$ and $g_r(\theta)$, respectively. $g(r)$ is 1 for a random distribution of $N_b$ bubbles whereas $g(r) < 1$ and $g(r) > 1$ represent a lower and a higher likelihood of two bubbles being separated by a distance $r$ (compared to a random distribution), respectively. For $r$ of the order of the bubble diameter, $g_r(\theta)$ accounts for the direct interaction of bubbles that are close. For large values of $r$, it is indicative of large-scale structure formation. For the calculation procedures of these quantities, see, Esmaeeli & Tryggvason (2005).

In the left frame of figure (7) we show $g(r)$ as a function of $r/a$ ($a$ is the bubble radius and these results were obtained by considering shells of $\Delta r = 0.25a$ thickness and averaging over 100 evenly spaced time samples in the $[t_s,\ t_f]$ time interval, where $t_s$ and $t_f$ are the end of the transient and the simulation time, respectively). For the spherical system at the high Reynolds number, $g(r)$ is zero only for $r/a < 1.37$ which highlights that the bubbles are slightly deformed. There is a strong peak at

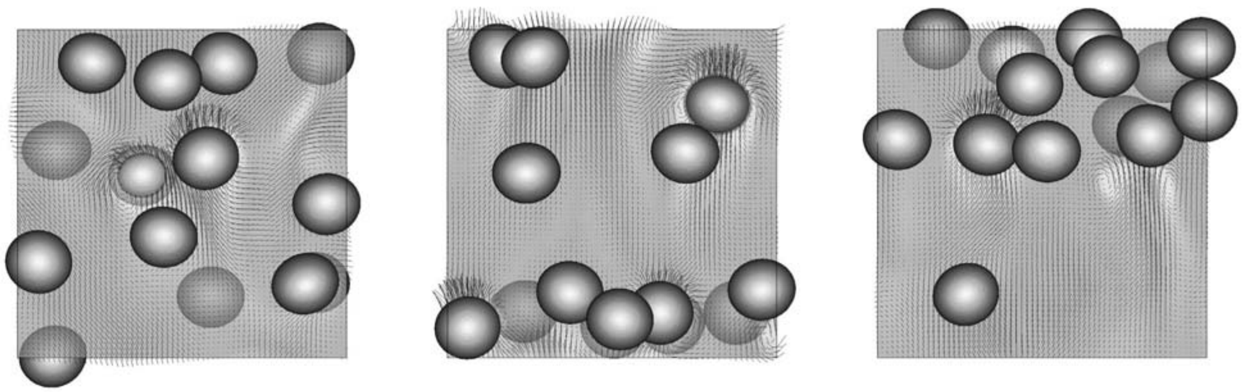

**Figure 5** : Breakup of a columnar array of 14 bubbles at $Eo = 0.5$ and $Mo = 1.95 \times 10^{-9}$. The figure shows the bubbles, the velocity vectors, and the vorticity field after the break up, and at two subsequent corresponding to quasi steady-state conditions.

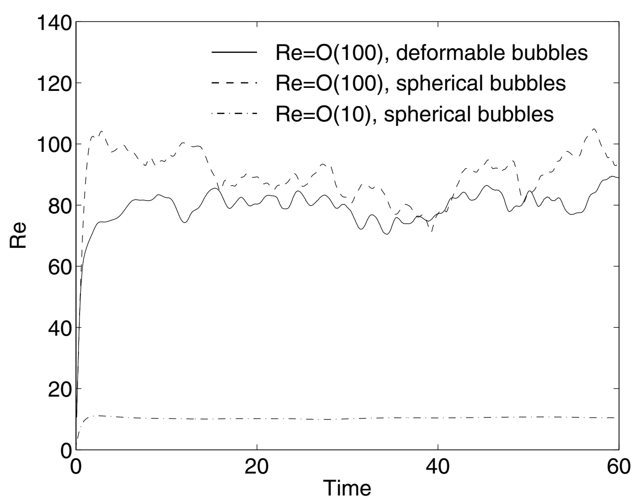


**Figure 6** : Comparison of the mean rise velocities of 14 bubbles, randomly distributed initially, at $Eo = 0.5$, $Mo = 10^{-6}$, $Eo = 4$, $Mo = 10^{-6}$, and $Eo = 0.5$, $Mo = 1.95 \times 10^{-9}$. These Eötvös and Morton numbers correspond to $Re = O(10)$ spherical bubbles, $Re = O(100)$ deformable bubbles, and $Re = O(100)$ spherical bubbles, respectively.

about $r/a = 2$ which shows a possibility of pairing of the bubbles. For the spherical system at the low Reynolds number, $g(r)$ is zero only for $r/a < 2.37$, which highlights that the bubbles remain spherical and also they do not touch. The peak shifts to about $r/a = 3.8$. For the deformable system, $g(r)$ is only zero at separation distances of $r/a < 0.87$ which highlights that the bubble deformation provides an incentive for bubbles to pair. Compared to the spherical bubbles, there is not a strong peak for the deformable system and the overall bubble distribution is fairly uniform. For all the cases, $g(r)$ drops down to 1 for $r/a > 5$ and remains relatively uniform thereafter.

The right frame of figure (7) shows $g_r(\theta)$ at $r = 2.5a$ as a function of $\theta$ for the systems of figure (6). $g_r(\theta)$ for the nearly spherical system at high Reynolds number shows a high probability to have side-by-side (i.e., $\theta = \pi/2$) bubbles in near contact conditions and a less probability for pair of bubbles to be in tandem (i.e., $\theta = 0$ or $\pi$). On the other hand, $g_r(\theta)$ for the deformable bubbles indicates a high probability for having tandem bubbles in near contact condition and a less probability of having side-by-side bubble pairs. This distribution is similar to that of Bunner & Tryggvason (2003) for deformable bubbles before the streaming state. For the spherical bubbles at low Reynolds number, we do not see a strong preference for bubbles to orient side-by-side or tandem as is evidenced by the figure which shows small peaks close to $\theta = 0, \pi$ and $\theta = \pi/8$.

In summary, the current simulations for spherical bubbles at O(10) and O(100) along with the results of Bunner & Tryggvason (2002$a$) at $Re \simeq 22$, suggest that there is a

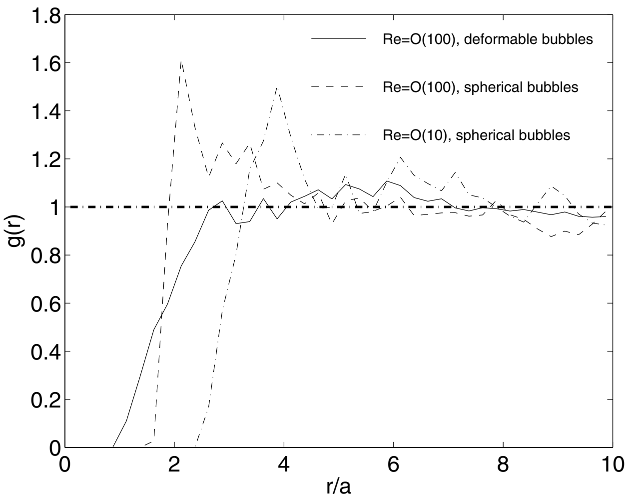


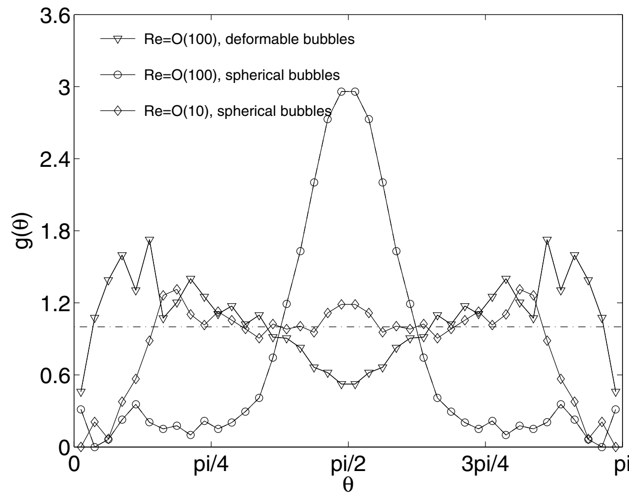


**Figure 7** : Radial $g(r)$ pair distribution (left) and angular pair distribution $g_r(\theta)$ (right) for the 14 bubbles simulations of figure (6). $g_r(\theta)$ is plotted for a separation distance of $r = 2.5a$, where $a$ is the bubble radius.

monotonic trend from the state of no-preference found by Ladd (1993) for Stokes flow, toward the strong layer formation seen in the potential flow simulations of Sangani and Didwania (1993) and Smereka (1993).

### *4.2 Thermocapillary-driven migration of bubbles*

In this section, we present some preliminary results of computations of thermocapillary-driven motion of bubbles. The simulations are done in a domain that is periodic in the horizontal direction and wall-bounded in the vertical direction. The temperature gradient is also in the vertical direction; upward or downward, depending on the problem. Here, we follow the motion until one of the bubbles becomes very close to the walls (at this point we stop the simulation). For this problem, there are several ranges of parameters that are of interest to the researchers in the field. For example, in glass melts (of interest for containerless glass processing in space; Uhlmann, 1982), $Pr = \nu_l/\alpha_l$ is typically $10^3$ or higher, the Reynolds number is around $10^{-8} - 10^{-2}$, and therefore, the Marangoni number $Ma = RePr$ can be relatively low or high (Satrape, 1992). Here, we do not focus on a particular fluid and instead work with a set of parameters which characterizes the motion at finite $Re_T$ and $Ma$. We are motivated by the fact that the motion in the limit of zero $Re_T$ and $Ma$ numbers is reasonably well-understood, and that the thermocapillary-driven motion of bubbles at finite $Re_T$ and $Ma$ is relevant to many practical applications. The investigation is limited to two-dimensional systems to resolve the flow better and to simulate motion of larger number of bubbles for a longer time. Compared with buoyancy-driven flows, thermocapillary-driven flows demand a higher grid resolution to accurately “capture” the motion at the phase boundary. Two-dimensional simulations do not provide results that can be expected to be in quantitative agreement with experiments, however, they can provide useful information about the “physics” of the considered phenomena.

We start by considering the behavior of 16 bubbles at $Re_T = 40$, $Ma = 40$, $Ca = 0.03$, $\alpha = 12.82\%$, and bubble/liquid material properties ratio of 0.5. The bubbles are initially set in the vertices of a $4 \times 4$ square. (These positions are then randomly disturbed). The first frame of figure (8) shows the initial positions of the bubbles and the subsequent frames show the bubbles and twenty equispaced streamlines. Since for the conditions considered here, the thermocapillary forces are relatively weak, the initial separation distance between the neighboring bubbles (on the average) is set to less than a bubble diameter to trigger faster interactions. The top wall is hot and the lower one is cold. Since the surface tension decreases with an increase in the temperature, this creates a downward force acting at the interfaces. The reaction to this force from the ambient fluid is upward and thus forces the bubbles to rise. The counter-rotating vortices seen inside the bubbles (second frame) pump the hot ambient liquid from the top to the bottom. The dividing streamlines of these vortices give the directions of the bubbles motions (which are mainly upward). Unlike

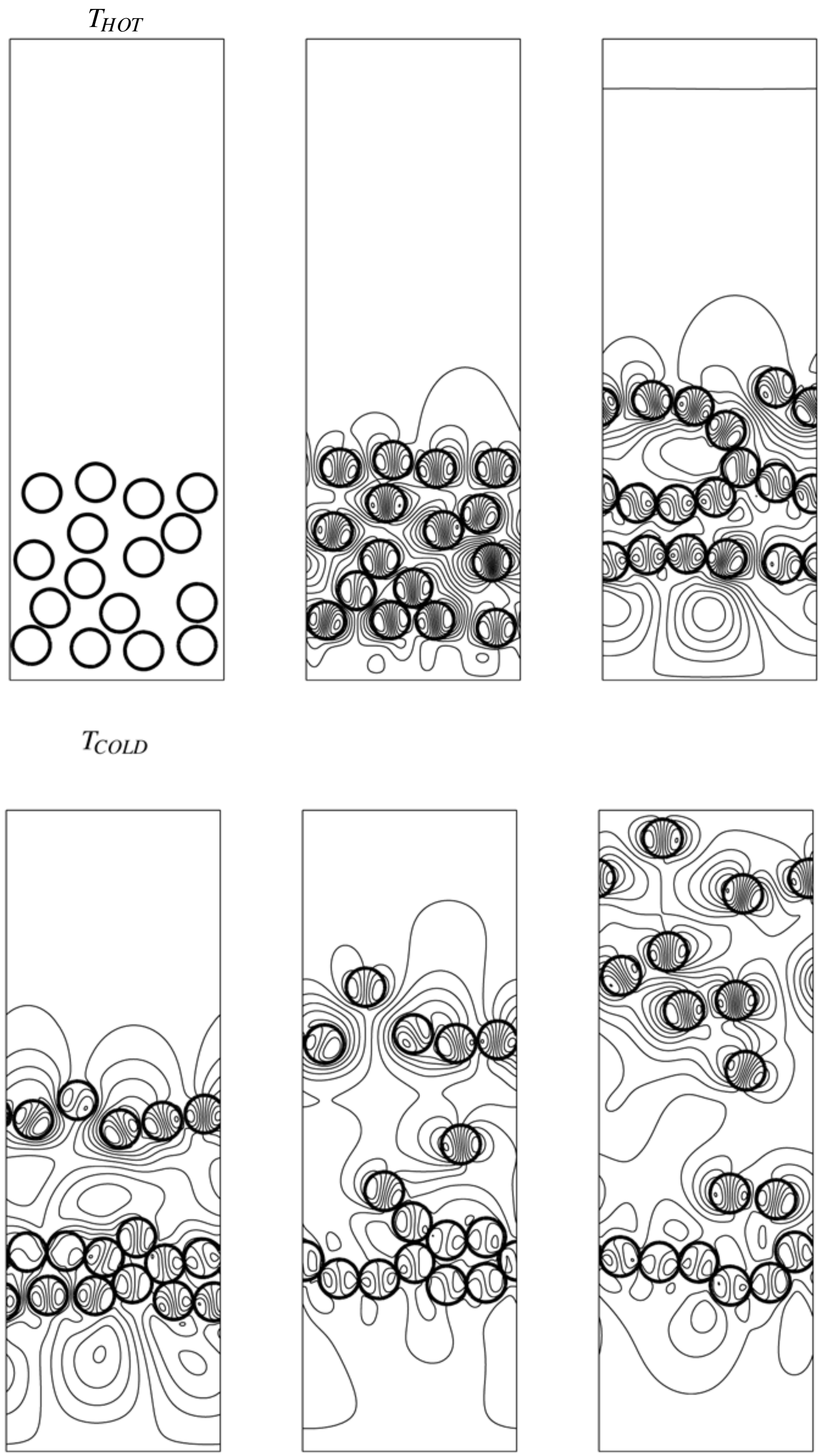


**Figure 8** : Thermocapillary migration of 16 bubbles in zero gravity. The figures show the bubbles and streamlines at selected times. The nondimensional parameters are $Re_T = 40$, $Ma = 40$, $Ca = 0.03$, and $\alpha = 0.128$. The domain size is $4 \times 12$ and is resolved by a $256 \times 768$ grid. Here, the upper wall is hot and the lower one is cold.

the buoyancy-driven flows where the direction of buoyant force is fixed, in thermocapillary-driven flows the direction of the driving force depends on the local temperature gradient. The smaller separation distance between the streamlines inside the bubbles compared with that of the ambient fluid is representative of the fact that the velocity is higher inside the bubbles. For a bubble that is in the wake of another one, as a result of the pumping of the hot liquid by the top bubble, already outlined in section 2.2, the temperature of the fluid in the gap between the bubbles will increase. This leads to a higher temperature gradient across the lower bubble and a lower temperature gradient across the upper one. As a result, the lower bubble eventually catches up with the top one. The bubbles, then tumble and rise side-by-side. The above mechanism leads to formation of horizontal layers of bubbles or "raft" (third frame). The raft formation leads to flow blockage, and consequently, to a decrease in the mean migration velocity. This mechanism can be highlighted by means of comparison of the streamlines in the third frame with those in the second one. The velocity decreases further as more bubbles participate in rafting (fourth frame). The touching state of bubbles, however, is not an equilibrium one, as the hot ambient fluid tends to flow around them. This leads to a local temperature gradient in the horizontal direction which results in the separation of bubbles (fifth frame). The last frame shows a more random distribution of the bubbles in the upper half of the domain while a raft is being destroyed in the lower half.

The mean rise velocity of the bubbles is an important parameter characterizing the overall behavior of the system and in figure (9) we show the evolution of this parameter. The velocity and the time have been scaled by $u_s = |\sigma_T \nabla T_\infty| a/\mu_l$ and $t_s = a/u_s$, respectively. For a bubble at these parameters, in the limit of zero $Re_T$ and $Ma$, equation (1) predicts a migration velocity of 0.228. We believe that the large difference between our migration velocity and that predicted by equation (1), leaving aside the two-dimensionality, is mainly due to the difference in the Marangoni number of the two systems. An increase in $Ma$, generally, leads to a decrease in the migration velocity as a result of generation of a more uniform temperature distribution around the bubble. Here, the velocity increases monotonically while the bubbles are rising up freely, but it starts to decrease as a result of the raft formation. The subsequent rise in the velocity is due to the

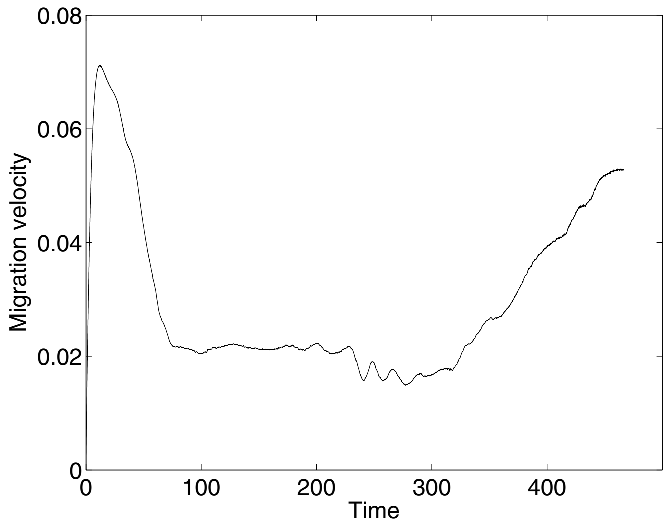


**Figure 9** : Evolution of the mean migration velocity (scaled by $u_s$) for the 16 bubbles shown in figure (8).

gradual destruction of the rafts.

While investigations of thermocapillary-driven flows in zero gravity lead to considerable insight into the dynamics of bubbles driven "solely" by temperature gradient, in many practical applications the buoyancy effects are not entirely absent. In the final part of this section we study the motion of bubbles under combined action of thermocapillary and buoyancy forces at finite $Re_T$ and $Ma$. This problem exhibits some interesting features when buoyancy and thermocapillary act in opposite directions. Before going any further, however, it is instructive to examine equation (1) in more detail. The first and the second terms in the parentheses are the contributions of the thermocapillary and the buoyancy forces, respectively. As a result, parameter $G_0$ formed by the ratio of these terms:

$$G_0 = \frac{3|\sigma_T \nabla T|}{\Delta\rho a(2+\eta)(1+\gamma)g},$$

characterizes the relative importance of thermocapillary and buoyancy effects. Note that $G_0$ is similar to $\Pi = |\sigma_T \nabla T_\infty|/\Delta\rho g a$ introduced earlier. For a single bubble in the limit of zero $Re_T$ and $Ma$, at $G_0 = 1$ the bubble remains stationary, and moves in the direction of thermocapillary (respectively buoyancy) for $G_0 > 1$ (respectively $G_0 < 1$).

As a first representative case we consider the motion of a single bubble at $Re_T = 5.0$, $Ma = 5.0$, $Ca = 0.033$, $\Pi = 0.74$, $\alpha = 0.07$, and the ratio of the material properties of 0.5. Since $\Pi < 1$, we expect the buoyancy to

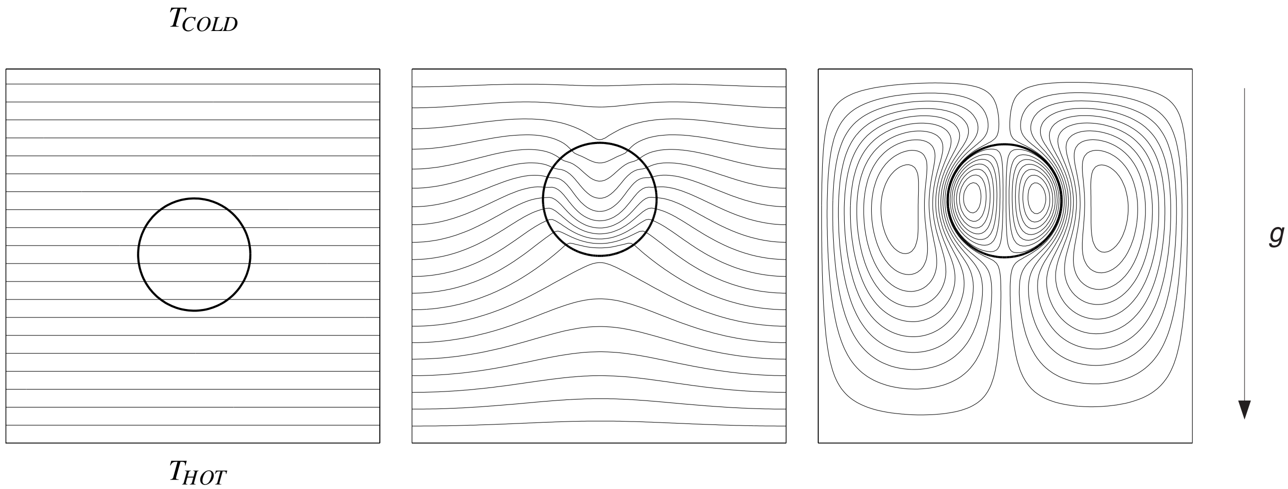


**Figure 10** : Bubble and the temperature contours at $t = 0$ (left frame), temperature contours (middle frame) and the streamline contours (right frame) at steady state conditions. Here, $Re_T = 5$, $Mo = 5$, $Ca = 0.033$, and $\Pi = 0.74$. The domain size is $1 \times 1$ and is resolved by a $128 \times 128$ grid. Here, both the temperature gradient and the gravity are downward.

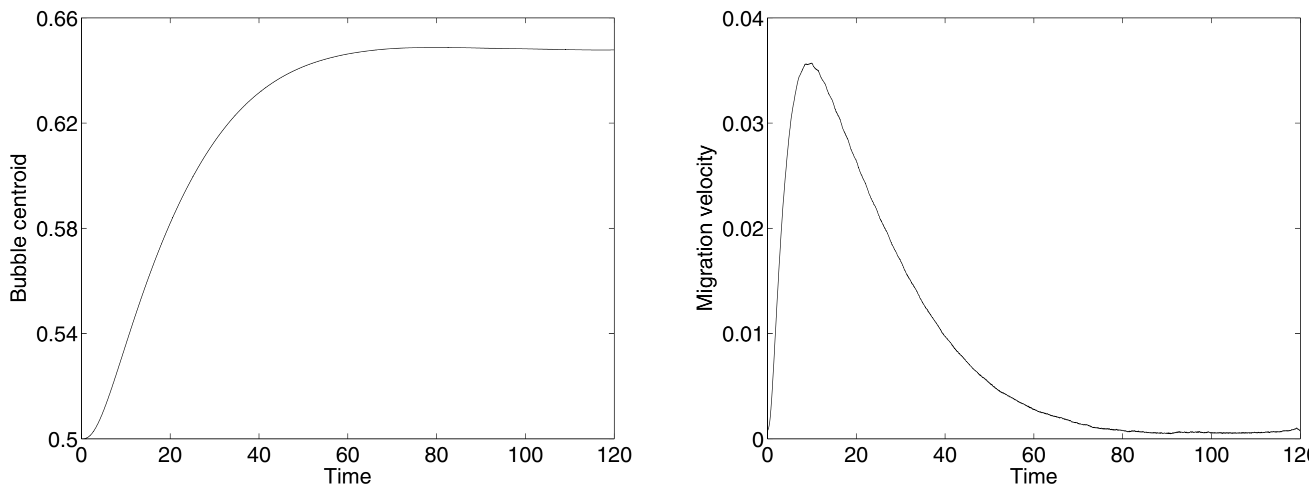


**Figure 11** : Motion of the centroid of the bubble in figure (10) (left frame) and its migration velocity (scaled by $u_s$) (right frame).

be more important. The bubble is set in the middle (i.e., $(x_c, y_c) = (0.5, 0.5)$) of a $1 \times 1$ domain and the flow is resolved by a grid resolution of $128 \times 128$. In terms of the bubble diameter, the domain is $3.3d_e \times 3.3d_e$ and the distance of the bubble centroid from the walls is $1.66d_e$. The gravitational acceleration is downward and the temperature gradient is downward too. So, the buoyancy tends to move the bubble upward while the thermocapillary tends to move it downward. The first frame of figure (10) shows the bubble and twenty equispaced temperature contours at $t = 0$. The subsequent frames show the bubble at steady state along with twenty equispaced temperature contours (middle) and streamlines (right frame). As is evidenced, the bubble has moved up slightly. Initially, the bubble velocity increases monotonically, however, it begins to decrease while the bubble has barely moved (i.e., $y_c = 0.53$). At this point the distance of the bubble centroid from the top wall is still about $1.5d_e$. The first frame of figure (11) shows the motion of the centroid of the bubble and the second frame shows the evolution of the migration velocity (scaled by $u_s$). At this stage additional simulations are required to discern the possible

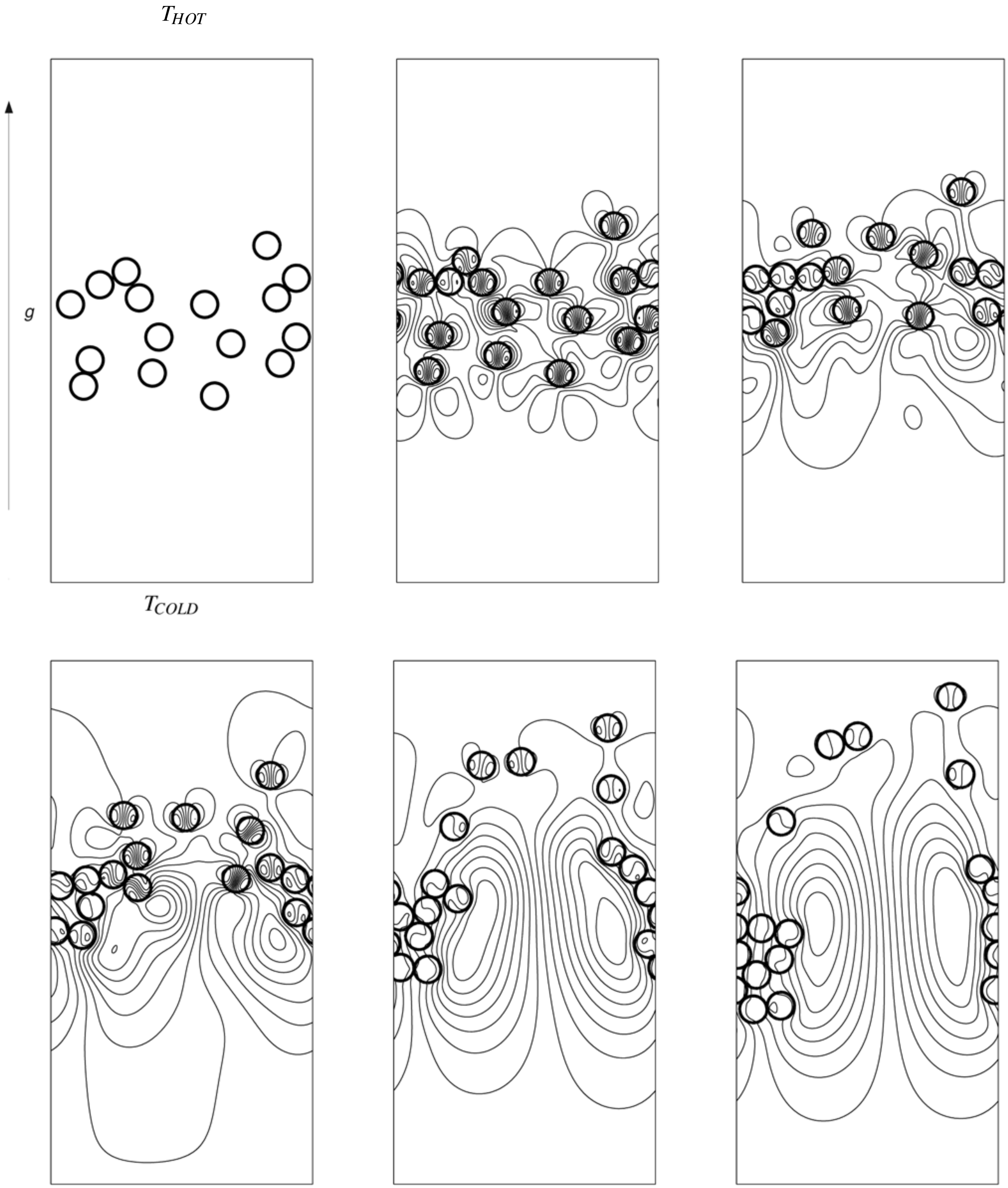


**Figure 12** : Evolution of 16 bubbles under combined effect of buoyancy and thermocapillary forces. The figures show the bubbles and streamlines at selected times. Here, to retain the same style used for figure 8, both the temperature gradient and the gravity are upward. The nondimensional parameters are $Re_T = 40$, $Ma = 40$, $Ca = 0.05$, $\Pi = 4.166$, and $\alpha = 0.0628$. The domain size is $4 \times 8$ and is resolved by a $256 \times 512$ grid. The nondimensional times are 0, 110.5, 313.2, 423,75, 718.5 and 939.65

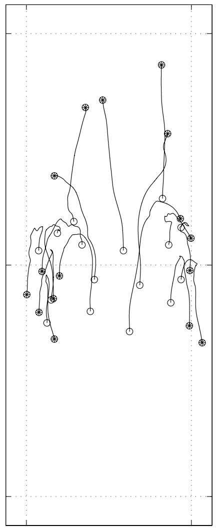

**Figure 13** : Trajectories of the bubbles in figure (12). The open circles mark the starting points and the filled ones mark the endpoints. Note that the size of the circles is not to scale.

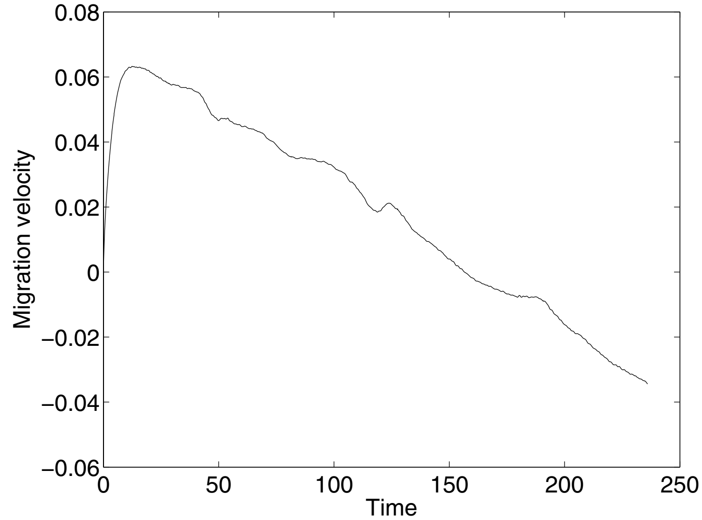


**Figure 14** : Evolution of the mean migration velocity (scaled by $u_s$) of the bubbles in figure (12).

role played in the behavior by "boundary wall effects." Within this context it is worthwhile to stress that in the limit of zero $Re_T$ and $Ma$, the velocity disturbance created by thermocapillarity dies off as $1/r^3$ while that of buoyancy dies off as $1/r$, where $r$ is the distance from the bubble (See, for example, Meyyappan *et al.*, 1981). Since the initial distance between the centroid and the upper wall is not large, it is possible that the motion due to buoyancy tends to be retarded by the upper wall from the very beginning, while that due to thermocapillary forces is unaffected. To discern if this is indeed the case, we have rerun the above simulation in the absence of the temperature gradient and observed that the bubble velocity is retarded by the upper wall only after the bubble has risen about half a diameter (i.e., $y_c = 0.64$). Since the bubble velocity in figure (11) decreases much earlier, we conclude that the bubble motion was not influenced by the wall.

To study the interactions of many bubbles under combined effects, we have performed a simulation of motion of 16 bubbles at $Re_T = 40$, $Ma = 40$, $Ca = 0.025$, $\Pi = 4.166$, $\alpha = 0.0628$, and bubble/liquid material properties ratio of 0.5. We use a $4 \times 8$ domain resolved by a $256 \times 512$ grid. Note that in figure ((12) to retain coherence with respect to the style used in Fig. 8, the temperature gradient and the gravity directions are both upward. The first frame shows the initial distribution of the bubbles and the subsequent frames shows the bubbles and twenty equispaced streamlines. Since the thermocapillary effect is dominant, the bubbles rise initially and also begin to form some local rafts. As the bubbles rise, they push down the hot ambient liquid around them. Here, the motion of the downcoming flow is accelerated by the buoyancy. While the motion in the surrounding field (i.e., in the vicinity of the bubbles) is determined by the thermocapillary effect, the motion in the far field (i.e., away from the bubbles) is dominated by the buoyancy. The outcome is a highly vortical flow where bubbles move upward while the ambient fluid, for the most part, moves downward. As a result, local vortices are generated in the ambient fluid which become larger and stronger over the time (second and third frames) and eventually form a large vortex (fourth frame; recall that the domain is periodic) which includes most of the bubbles. The bubbles at the edge of this vortex are pushed downward. It appears that thermocapillarity provides a necessary incentive for this cluster formation by its tendency for raft formation. Figure (13) shows the paths of the bubbles during the simulation which well correlate with the motion of the large vortex. Figure (14) shows the mean migration velocity (scaled by $u_s$) of the bubbles that exhibits a transition from thermocapillary-driven motion to a buoyancy-driven one.

## 5 Conclusion

Phase distribution of bubbles in buoyancy- and thermocapillary-driven flows was studied. For buoyant rise of spherical bubbles, the results suggest a monotonic trend from a "no-preference state" at $O(10)$ Reynolds number toward a strong layer formation at $O(100)$ Reynolds number. For deformable bubbles at $O(100)$ Reynolds number, however, the large-scale structure tends to be nearly uniform. For thermocapillary-driven motion of two-dimensional bubbles, the simulations suggest raft formation at zero gravity, and cluster formation when buoyancy acts in an opposite direction to thermocapillarity.

**Acknowledgement:** The buoyancy-driven part of this study was supported by the US Department of Energy under grant DE-FG02-03ER46083 and the thermocapillary part was supported by NASA Microgravity program under grant NAG3-1952. The simulations of three-dimensional flows were computed at the computers provided by the National Partnership for Advanced Computational Infrastructure (NPACI) under grant CTS010003.

## References

**Acrivos, A., Jeffry, D. J., and Saville, D. A.** (1990): Particle migration in suspension by thermocapillary or electrophoretic motion *J. Fluid Mech.*, vol. 212, pp. 95-110.

**Batchelor, G. K.** (1972): Sedimentation in a dilute dispersion of spheres *J. Fluid Mech.*, vol. 52, pp. 245-268.

**Balasubramaniam, R. and Chai, A.** (1987): Thermocapillary migration of droplets: An exact solution for small Marangoni numbers *J. Colloid. Interface Sci.*, vol. 119, pp. 531-538.

**Bossis, G. and Brady, J. F.** (1984): Dynamic simulation of sheared suspension. I. General method *J. Chem Phys.*, vol. 80, pp. 5141-5154.

**Brady, J. F. and Bossis, G.** (1985): The rheology of concentrated suspensions of spheres in simple shear flow by numerical simulation *J. Fluid Mech.*, vol. 155, pp. 105-129.

**Bunner, B. and Tryggvason, G.** (2003): Effect of bubble deformation on the properties of bubbly flows *J. Fluid Mech.*, vol. 495, pp. 77-118.

**Bunner, B. and Tryggvason, G.** (2002): Dynamics of homogeneous bubbly flows Part 1. Rise velocity and microstructure of the bubbles *J. Fluid Mech.*, vol. 466, pp. 17-52.

**Bunner, B. and Tryggvason, G.** (2002b): Dynamics of homogeneous bubbly flows Part 2. Velocity fluctuations *J. Fluid Mech.*, vol. 466, pp. 53-84.

**Clift, R., Grace, J. R., and Weber, M. E.** (1978): Bubbles, Drops, and Particles, Academic Press.

**Crespo, A. and Manuel, F.** (1983): Bubble motion under reduced gravity, Proc. 4th European Symposium on Materials Science under Microgravity, Madrid, Spain, pp. 45-49.

**Esmaeeli, A. and Arpaci, V.** (1999): Thermocapillary driven migration of bubbles in shear flows, paper number FEDSM99-7376, Proceedings of the ASME-FED summer meeting, July, pp. 18-23, San Francisco, CA.

**Esmaeeli, A. and Tryggvason, G.** (2005): A DNS study of the buoyant rise of bubbles at $\mathbf{O(100)}$ Reynolds number, *Phys. Fluids* (accepted).

**Esmaeeli, A. and Tryggvason, G.** (1999): Direct numerical simulations of bubbly flows. Part II-Moderate Reynolds number arrays *J. Fluid Mech.*, vol. 385, pp. 325-358.

**Esmaeeli, A. and Tryggvason, G.** (1998): Direct numerical simulations of bubbly flows. Part I-Low Reynolds number arrays *J. Fluid Mech.*, vol. 377, pp. 313-345.

**Esmaeeli, A., Tryggvason, G., and Arpacı, V.** (1997): Thermocapillary Migration of Bubbles in Shear Flow. Paper Number FEDSM97-3523, ASME Proceedings of the 1997 ASME (FED) Summer Meeting, June 22-27, 1997, Vancouver, Canada. Editor: Tim O'hern.

**Esmaeeli, A., Tryggvason, G., and Arpacı, V.** (1996): Thermal Migration of Bubbles in Zero Gravity. Heat Transfer in Microgravity Systems, Editors: A. Gopinath and S. S. Sadhal, HTD-Vol. 332 (ASME, Atlanta, Georgia, 1996), pp. 55-63.

**Fortes, A. F., Joseph, D. D., and Lundgren, T. S.** (1987): Nonlinear mechanics of fluidization of beds of spherical particles *J. Fluid Mech.*, vol. 177, pp. 467-483.

**Happel, J. and Brenner, H.** (1965): Low Reynolds number hydrodynamics, Prentice-Hall.

**Harper, J. F.** (1973): On bubbles with small immobile adsorbed films rising in liquids at low Reynolds numbers *J. Fluid Mech.*, vol. 58, pp. 539-545.

**Kim, S. and Karrila, S. J.** (1991): Microhydrodynamics: principles and selected applications, Butterworth-Heinemann.

**Ladd, A. J. C.** (1993): Dynamical simulations of sedimenting spheres *Phys. Fluids A*, vol. 5, pp. 299-310.

**Lamb, H.** (1932): Hydrodynamics, Dover, New York.

**Lappa, M.** (2005): Assessment of VOF strategies for the analysis of Marangoni Migration, collisional coagulation of droplets and thermal wake effects in metal alloys *Computers, Materials & Continua*, vol. 2, pp. 51-64.

**Meyyappan, M., Wilcox, W. R., and Subramanian, R. S.** (1981): Thermocapillary migration of bubbles normal to a plane surface. *J. Colloid. Interface Sci.* vol. 83, pp. 199-208.

**Nas, S. and Tryggvason, G.** (2003): Thermocapillary interaction of two bubbles or drops *Int. J. Multiphase Flow*, vol. 29, pp. 1117-1135.

**Nas, S.** (1995): Computational investigations of thermocapillary migration of bubbles and drops in zero gravity, Ph.D. Thesis, The University of Michigan.

**Nas, S. and Tryggvason, G.** (1993): Computational investigation of the thermal migration of bubbles and drops. Proceedings of the ASME Winter annual meeting, FED-175, pp. 71-83.

**Ostrach, S.** (1982): Low-gravity fluid flows. *Ann. Rev. Fluid Mech.*, vol. 14, pp. 313-345.

**Sangani, A. S. and Didwania, A. K.** (1993): Dynamic simulations of flows of bubbly liquids at large Reynolds numbers *J. Fluid Mech.*, vol. 250, pp. 307-337.

**Satrape, J. V.** (1992): Interactions and collisions of bubbles in thermocapillary motion *Phys. Fluids A*, vol. 4, pp. 1883-1900.

**Smereka, P.** (1993): On the motion of bubbles in a periodic box *J. Fluid Mech.*, vol. 254, pp. 79-112.

**Stewart, C. W.** (1995): Bubble interaction in low-viscosity liquids *Int. J. Multiphase Flow*, vol. 21, pp. 1037-1046.

**Subramanian, R. S.** (1992): The motion of bubbles and drops in reduced gravity, In: Chabra, R. P. and De Kee, D. (Eds.), Transport processes in bubbles, drops, and particles, Hemisphere publishing co. Washington, D.C., USA, pp. 1-42.

**Uhlmann, D. R.** (1982): Glass processing in a Microgravity Environment. In: Rindone, G. E. (Ed.), Materials Processing in the Reduced Gravity Environment of Space, Elsevier, New York, USA, pp. 269-278.

**Unverdi, S. O. and Tryggvason, G.** (1992): A front-tracking method for viscous, incompressible, multi-fluid flows *J. Comput. Phys.*, vol. 100, pp. 25-37.

**Weatherburn, C. E.** (1927): Differential geometry of three dimensions, Cambridge University Press, vol. I.

**Young, N. O., Goldstein, J. S., Block, M. J.** (1959): The motion of bubbles in a vertical temperature gradients *J. Fluid Mech.*, vol. 6, pp. 350-356.

**Zhou, H. and Pozrikidis, C.** (1994): Pressure-driven flow of suspensions of liquid drops *Phys. Fluids*, vol. 6, pp. 80-94.